Sonic boom propagation over real topography

Ariane Emmanuelli, Didier Dragna, S. Ollivier, Philippe Blanc-Benon

JASA ARTICLE

Sonic boom propagation over real topography

Ariane Emmanuelli, Didier Dragna,[a] Sébastien Ollivier, and Philippe Blanc-Benon
Univ Lyon, Ecole Centrale de Lyon, CNRS, Univ Claude Bernard Lyon 1, INSA Lyon, LMFA, UMR5509, 69130, Ecully, France

ABSTRACT:
The effect of elevation variation on sonic boom reflection is investigated using real terrain data. To this end, the full two-dimensional Euler equations are solved using finite-difference time-domain techniques. Numerical simulations are performed for two ground profiles of more than 10 km long, extracted from topographical data of hilly regions, and for two boom waves, a classical *N*-wave, and a low-boom wave. For both ground profiles, topography affects the reflected boom significantly. Wavefront folding due to terrain depression is notably highlighted. For the ground profile with mild slopes, the time signals of the acoustic pressure at the ground are, however, only slightly modified compared to the flat reference case, and the associated noise levels differ by less than 1 dB. With steep slopes, the contribution due to wavefront folding has a large amplitude at the ground. This results in an amplification of the noise levels: a 3 dB increase occurs at 1% of the positions along the ground surface, and a maximum of 5–6 dB is reached near the terrain depressions. These conclusions are valid for the *N*-wave and low-boom wave.
 https://doi.org/10.1121/10.0019938

(Received 14 March 2023; revised 9 June 2023; accepted 12 June 2023; published online 5 July 2023)

[Editor: Olga Umnova] Pages: 16–27

I. INTRODUCTION

Sonic boom is one of the main issues of concern in the field of supersonic civil transport. Indeed, overland civil supersonic flight was banned in the 1970s because of the public annoyance caused by the boom. The ban is still in effect today. The feasibility of an aircraft design generating reduced boom has been confirmed experimentally (Pawlowski *et al.*, 2005) and should be further demonstrated in coming years (NASA, 2022). This may open the way to the lift of the ban, in which case regulatory authorities will set a maximum level for overland sonic boom to limit the population disturbance. To support these regulations, it is, thus, important to identify environmental parameters that affect the boom at the ground and estimate the induced variability of noise levels and the corresponding occurrence. Such work is in progress for atmospheric stratification (Blumrich *et al.*, 2005; Leal *et al.*, 2021; Yamashita and Obayashi, 2013) and atmospheric turbulence (see, e.g., the recent studies of Carr *et al.*, 2022; Leconte *et al.*, 2022; Stout *et al.*, 2021), but this remains to be investigated for topography.

Indeed, reflection of sonic boom over non-flat terrain has received little attention in the literature (Maglieri *et al.*, 2014). Experiments at laboratory scale have been reported in Bauer and Bagley (1970), using the firing of model projectiles to create *N*-waves. Reflection of sonic boom on a surface in the form of a paraboloid of revolution was investigated. The authors note that concave topographical shapes can induce a large increase in the boom duration and peak pressure (a factor of 13.8 was measured at the parabola focal point). Recently, Emmanuelli *et al.* (2021) have performed a numerical study to characterize the topographic effects on sonic boom reflection. To do so, simple terrain profiles were considered, namely, a terrain depression, hill, and sinusoidal terrain. The study showed the significance of focusing induced by topography. For isolated terrain irregularities, pressure waveforms at ground level were not only made of the incident boom and its reflection but also a contribution due to wavefront folding. The latter appears as a *U*-wave with an incident *N*-wave. For a sinusoidal terrain, several additional contributions were noted on the waveforms due to the repeated folding of the wavefront. Compared to the flat case, the increase in noise levels was of several decibels. Finally, the variations of the perceived noise levels were similar for the *N*-wave and low-boom wave. Note that the waveforms reported in Bauer and Bagley (1970) for the paraboloid of revolution were also composed of an *N*-wave followed by a *U*-wave.

This paper continues the work of Emmanuelli *et al.* (2021) by considering real topography and aims at investigating the effect of realistic elevation variations on sonic boom reflection. To do so, variations in pressure signals are analyzed at ground level, and perceived noise is quantified for two terrain profiles illustrative of hilly regions.

The paper is organized as follows. Section II details the configurations and methodology. A geometrical analysis of the impact of topography on boom reflection depending on the terrain slope is presented in Sec. III. Results of the numerical simulations are then considered in Sec. IV, first for a ground profile presenting mild slopes and then for a ground profile with steep slopes. The distribution of the

[a]Electronic mail: didier.dragna@ec-lyon.fr

 0001-4966/2023/154(1)/16/12/$30.00

https://doi.org/10.1121/10.0019938

perceived noise levels is also discussed. Finally, concluding remarks are given in Sec. V.

II. METHODOLOGY AND CONFIGURATIONS

Sonic boom propagation over real topography is investigated using numerical simulations. Two-dimensional (2D) geometries are considered, hence, neglecting any variation in terrain elevation in the transverse direction. As sketched in Fig. 1, the aircraft is flying from left to right. To focus on topography, the atmosphere is homogeneous and at rest with the air density set to $1.22\,\mathrm{kg\,m^{-3}}$ and the ambient sound speed set to $c_0 = 340\,\mathrm{m\,s^{-1}}$. In addition, the ground surface is perfectly reflecting.

A. Methodology

The 2D Euler equations are solved in curvilinear coordinates using high-order finite-difference time-domain techniques (Bogey and Bailly, 2004). The solver has recently been used to study sonic boom reflection over non-flat terrain (Emmanuelli *et al.*, 2021) and urban environments (Dragna *et al.*, 2022a,b). It is described in detail in Emmanuelli *et al.* (2021), and its main characteristics are summarized in the following for completeness.

The terrain-following transformation from curvilinear coordinates (ξ,η) to Cartesian coordinates (x,z), proposed by Gal-Chen and Sommerville (1975), is used to account for non-flat terrain. A moving frame technique is implemented to reduce the computational cost: instead of computing the flow variables in the entire region of interest, the computational domain is restricted to a comparatively narrow region that follows the incident boom. The latter is imposed as the right boundary condition using the pressure waveform and isentropic relations. A perfectly matched layer is implemented at the top boundary as a nonreflecting boundary condition. At the ground, a rigid boundary condition is imposed by setting the normal velocity to zero. Finally, a nonreflecting boundary condition is not needed at the left boundary: as the moving frame moves at supersonic speed, the acoustic waves leave the computational domain without generating spurious reflected waves.

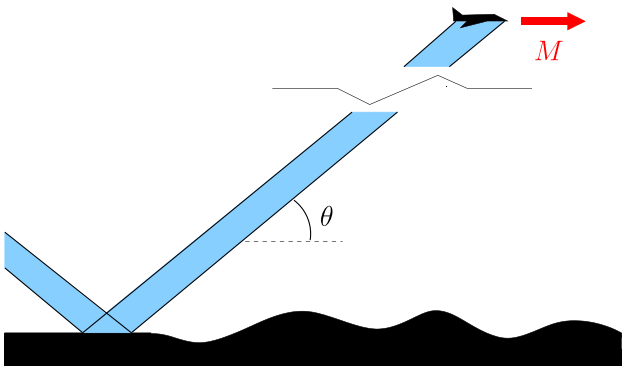

FIG. 1. (Color online) Sonic boom propagation over non-flat terrain from an aircraft flying at a Mach number M.

The two incident boom waves already used in the previous studies by Dragna *et al.* (2022a,b) and Emmanuelli *et al.* (2021) are considered: a classical N-wave and a low-boom wave. The corresponding waveforms of the acoustic pressure, p', are plotted as a function of time, t, in Fig. 2. The N-wave has a peak value equal to 24 Pa, a rise time of 0.0011 s, and a duration of 0.15 s, corresponding to a characteristic wavelength of 51 m. The low-boom wave, referred to as C25D, originates from a notional aircraft design, which was used in the 2nd AIAA Sonic Boom Workshop (Rallabhandi and Loubeau, 2019). It was obtained by propagating the near-field signature down to the ground using the BANGV nonlinear ray tracing code (Loubeau and Coulouvrat, 2009). The C25D wave has a peak value of 20 Pa, a rise time of 0.014 s, and a duration of about 0.1 s, corresponding to a characteristic wavelength of 34 m. Although the frequency content of the N-wave is significant up to a few kHz, that of the C25D wave is restricted to lower frequencies, with negligible energy above 800 Hz. In addition, the flight Mach number is set to $M = 1.6$. The sonic boom incidence angle with respect to the horizontal θ, given by $\sin\theta = 1/M$, is, thus, equal to 38.7°.

Perceived noise levels, L, are estimated using two metrics: Stevens' Mark VII perceived level (PL) (Stevens, 1972), which was shown to be the best suited for sonic boom in Leatherwood *et al.* (2002), and the C-weighted sound exposure level (CSEL), which gives more importance to low frequencies. Note that other metrics are also used to describe noise annoyance caused by sonic booms, namely, ASEL, BSEL, DSEL, ESEL, and ISBAP (Loubeau *et al.*, 2015). Emmanuelli *et al.* (2021) showed that these seven metrics yield comparable variations of boom levels due to topography. In the following, the values of perceived noise levels determined with the PL and CSEL metrics are given in PLdB and dBC, respectively.

B. Configurations

Two ground profiles, which have been extracted from topographical data provided by the French National Geographic Institute (IGN, Institut national de l'information géographique et forestière), are investigated. The ground profiles have been chosen with five constraints in mind. First, elevation variations should be large enough to expect

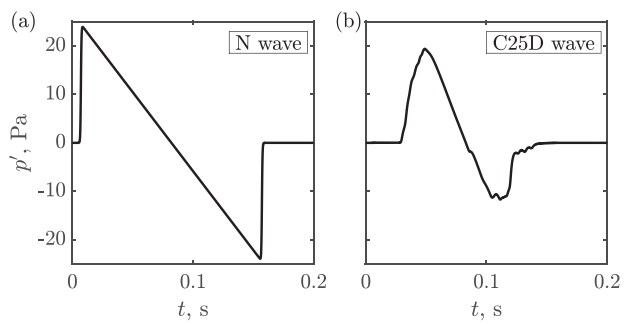

FIG. 2. Time signals of the incident boom for the (a) N-wave and (b) C25D wave.

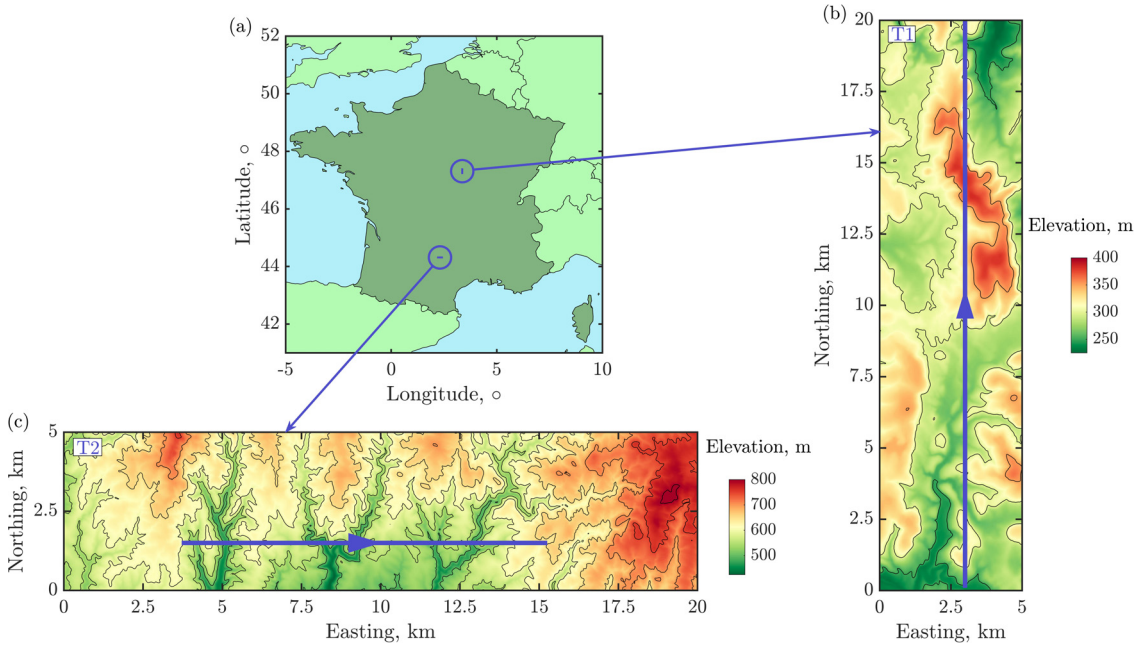

FIG. 3. (Color online) (a) Position of the two selected profiles on the map of Metropolitan France and topographic maps including profiles (b) T1 and (c) T2 are shown. In (b) and (c), the profiles are plotted in thick blue solid lines, and 50 m contour lines are drawn in thin black lines. The direction of flight is indicated by arrows.

noticeable effects on the boom. Second, the profiles must be continuous because of the curvilinear transformation used. Regions with cliffs or ravines have, thus, been avoided. Third, the difference between the minimum and maximum elevations should not be too large (about 100 m) such that the height of the computational domain and computational cost of the numerical simulations remain reasonable. Therefore, mountainous regions have been discarded. Fourth, the profiles should be long enough to perform a statistical analysis. Fifth, the resolution should be as fine as possible to capture the small scales of topography.

The location of the two ground profiles is shown on the map of France in Fig. 3. The ground profiles, denoted thereafter as T1 and T2, are presented in Fig. 4, where (x,z) are the Cartesian coordinates in the vertical plane containing the ground profile. Note that the horizontal resolution of the topographical data is 5 m and the vertical resolution is 0.1 m. In addition, the elevation height has been shifted such that the minimum value is zero.

The ground profile, T1, is 20 km long and has been extracted from the Nivernais region [47.22° N, 3.33° E] in central France. It can be roughly divided into three parts. The first part, noted T1a, for $x < 8$ km, consists of long hills with gentle slopes (around 15%–20%), whereas the second part, noted T1b, for x between 8 and 15 km is almost flat. The third part, noted T1c, for $x > 15$ km, is made of hills with medium slopes (20%–30%). The ground profile T2, which is 11 km long, has been extracted from the Ségala region [44.29° N, 2.19° E] in southern France. It is composed of a plateau cut by valleys with steep slopes (between 50% and 80%). The longest flat portions of the plateau are located between 2 and 4 km and 6.2 and 8 km.

Both profiles present similar elevation variation with standard deviation of the elevation height equal to 32.5 m and 42.4 m for T1 and T2, respectively. The main difference is in the slope variation, which is greater for profile T2 than for T1: the standard deviation of the slope is equal to 8.1% for T1 and 20.6% for T2.

C. Simulation parameters

The moving frame in the curvilinear coordinate system (ξ, η) is 600 m long and 500 m high. The mesh is uniform with a grid step $\Delta\xi = \Delta\eta = 0.1$ m, yielding a computational

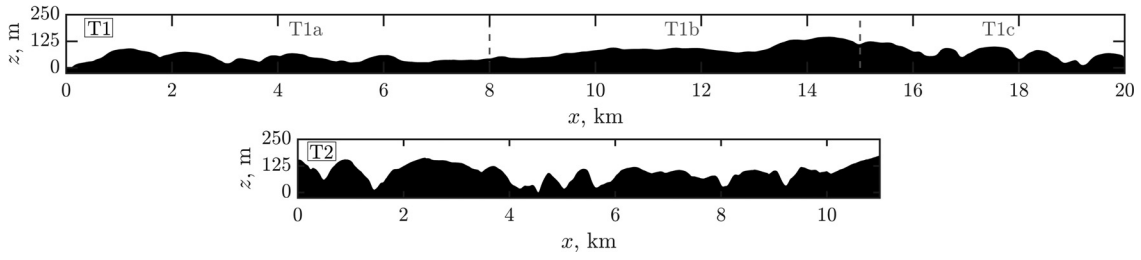

FIG. 4. Ground profiles T1 and T2. The scale along the z axis is magnified by a factor of 4 to highlight variations in elevation height.

https://doi.org/10.1121/10.0019938

domain of 30×10^6 points. Note that the entire domain, of length equal to 20 km for ground profile T1 and 11 km for T2, contains 1×10^9 and 550×10^6 grid points, respectively. Thus, the moving frame allows for a reduction in mesh size by a factor of 33 for T1 and a factor of 18 for T2, which shows the relevance of the moving frame approach to reduce computational cost. Also, as the grid step is smaller than the horizontal resolution of the elevation data, the ground profile is obtained by piecewise cubic interpolation in the simulations.

The moving frame is shifted by one spatial step every two time iterations. The time step is set to $\Delta t = \Delta\xi/(2Mc_0)$ such that the incident boom is stationary in the moving frame; this yields $\Delta t = 9.2 \times 10^{-5}$ s. The Courant–Friedrichs–Lewy (CFL) number, defined by $\mathrm{CFL} = c_0\Delta t/\Delta\xi$ is, thus, equal to $\mathrm{CFL} = 1/(2M) = 0.3125$. The simulation time required for the incident boom to propagate over the length of the ground profile is 36.6 s for T1 and 20.2 s for T2. This corresponds to 4×10^5 iterations for T1 and 2.2×10^5 iterations for T2. Simulations are run using 32 core nodes of Intel Skylake with a clock frequency of 2.6 GHz. The computational time is around 8100 central processing unit (CPU) hours for T1 and 4300 CPU hours for T2.

Note that a convergence study is included in Emmanuelli *et al.* (2021) to determine the grid resolution required for accurate noise prediction using different metrics. It was presented that 0.1 m is sufficient to estimate levels from PL and CSEL metrics with the C25D wave. However, with the *N*-wave, PL requires a smaller grid cell size while the levels are accurately estimated with CSEL with a spacing of 0.1 m. Consequently, noise levels will be computed using PL and CSEL in the case of the C25D wave and only CSEL with the *N*-wave. The noise levels at ground level for a perfectly reflecting flat ground surface, denoted by $L(\mathrm{flat})$, are used as a reference, and they are equal to 103.2 dBC for the *N*-wave and 83.2 PLdB and 97.2 dBC for the C25D wave.

III. GEOMETRICAL ANALYSIS

Before considering the simulation results, a geometrical analysis is made of the sonic boom reflection over non-flat terrain.

First, in Fig. 5, consider an incident boom propagating over a surface of constant slope. As sketched in Fig. 5(a), the angle between the boom wavefront and the horizontal is denoted by θ and it relates to the Mach number via $\sin\theta = 1/M$. Assuming specular reflection, the angle of the reflected boom wavefront with respect to the horizontal is given by $\theta - 2\alpha$, where α is the slope angle. For a horizontal ground surface ($\alpha = 0$) such as in Fig. 5(b), it is, thus, equal to θ. The reflected boom wavefront is rotating closer to the incident wavefront in the case of a downward slope ($\alpha < 0$), as depicted in Fig. 5(c), and away from it with an upward slope ($\alpha > 0$), as represented in Fig. 5(d).

Two limiting cases are identified. For $\alpha < \theta - \pi/2$ (or a slope $\tan\alpha < -\sqrt{M^2 - 1}$), the incident boom cannot reflect

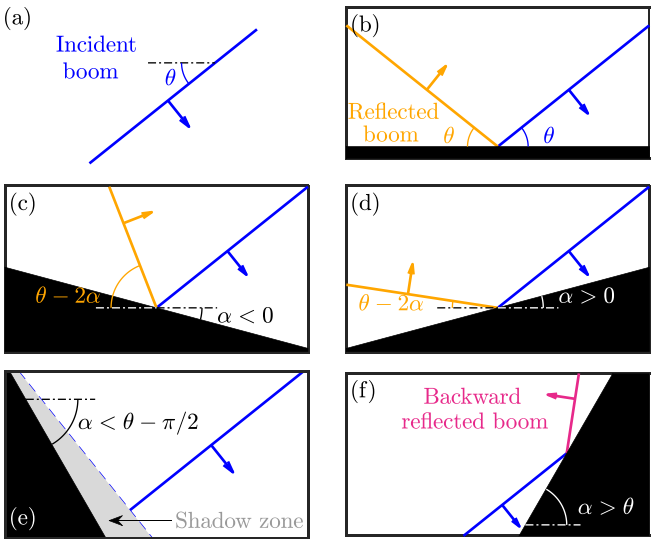

FIG. 5. (Color online) Geometrical analysis of sonic boom propagation over non-flat terrain showing (a) incident wavefront and its reflection (b) from a horizontal ground surface, and (c)–(f) from a ground surface of constant slope. See the text for details.

on the ground and a shadow zone is formed close to the ground surface, as illustrated in Fig. 5(e). For $\alpha > \theta$, corresponding to a slope $\tan\alpha > 1/\sqrt{M^2 - 1}$, the ground surface acts as a barrier and the boom is reflected backwards, as sketched in Fig. 5(f). Note that for the Mach number under consideration ($M = 1.6$), these two phenomena require large slopes: backward reflection occurs for slopes larger than 80% and shadow zones occur for slopes smaller than −125%. For both profiles (even for T2), the slope does not reach these values. Note, however, that this can occur for a topography with cliffs, ravines, or mountains.

Let us now analyze how slope variations affect boom reflection. To do so, we consider sonic boom propagation over corners and terrain depressions in Fig. 6. For each case considered, the wavefront is represented at three instants in time.

First, in Figs. 6(a)–6(d), we consider the propagation of a plane wavefront over a corner with a horizontal section on the left. In the case of a sharp convex corner in Fig. 6(a), the angle of the reflected wavefront is increased in the downslope part compared to the horizontal. The reflected boom wavefront in the downslope part propagates away from the reflected wavefront in the horizontal part, which yields a discontinuous wavefront. Therefore, a shadow zone for the reflected boom is formed in an angular sector centered at the corner and located between the angles $\pi/2 - \theta$ and $\pi/2 - \theta + 2\alpha$.

For a rounded convex corner with a continuously varying slope in Fig. 6(b), the angle of the reflected wavefront follows that of the ground profile, yielding a continuous and diverging wavefront. Thus, there is no shadow zone, but the amplitude of the reflected boom is expected to be reduced in the region included between the two dashed lines in Fig. 6(b) due to the divergence of the wavefront.

For a sharp concave corner in Fig. 6(c), the wavefront is also discontinuous. However, in this case, the reflected

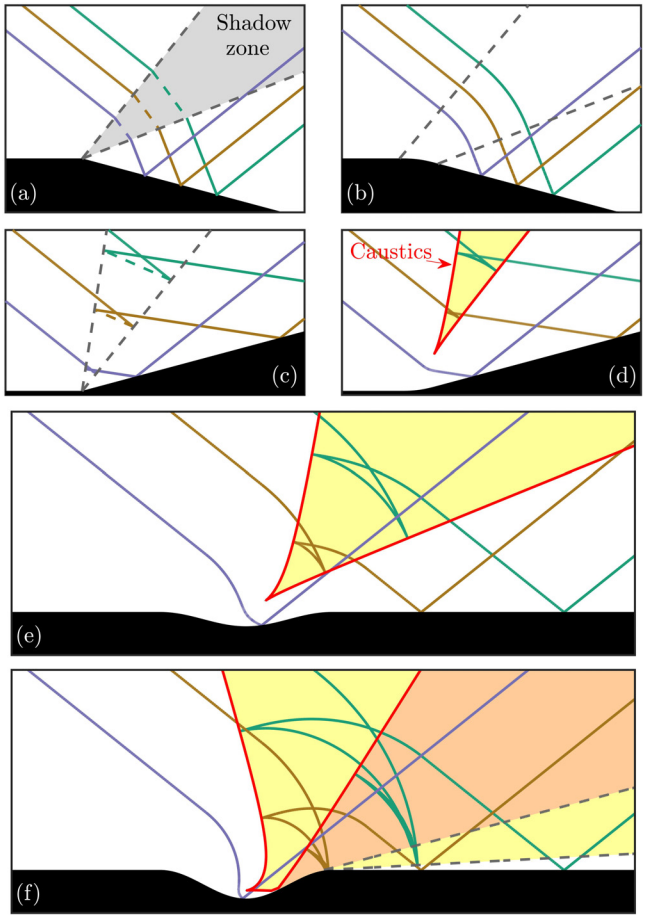

FIG. 6. (Color online) Geometrical analysis of sonic boom propagation over a non-flat terrain showing (a)–(d) reflection from a corner and (e)–(f) from a terrain depression. The wavefront is represented at three instants in time for each case. The illuminated zones of the caustics are colored in yellow in regions where there are three contributions to the reflected wavefront and in orange where there are five contributions.

wavefront in the upward slope propagates into the reflected wavefront in the horizontal part. There are, thus, two reflected booms in the angular sector centered at the corner bounded by the two dashed lines with slope angles $\pi/2 - \theta$ and $\pi/2 - \theta + 2\alpha$.

For a rounded concave corner in Fig. 6(d), the reflected wavefront is first continuous near the ground. Because of the ground surface concavity, the wavefront is converging. As it propagates, it converges at the focal point and then folds on itself with a characteristic pattern that resembles a butterfly or a fish tail. The caustics are the curves along which the wavefront is folding. They appear, in this example, as a cusp caustic. In the region bounded by the caustics, termed the illuminated zone, there are now three components to the reflected boom, the first two related to the reflection on the horizontal and upward slopes and the third related to the wavefront folding. The amplitude of the sound pressure is expected to be large at the focal point of the converging wavefront, corresponding to the caustic cusp, and along the caustics. Note that the acoustic field is continuous through the caustics; in the shadow zone of the caustic, which is the zone outside of the illuminated zone, the amplitude of the acoustic pressure decreases exponentially away from the caustic with a decay rate that depends on the frequency among others. Therefore, the impact of wavefront folding is also noticeable outside of the illuminated zone of the caustics. The process of wavefront folding due to the reflection from a concave ground profile is similar to that resulting from propagation in a turbulent atmosphere, discussed, for instance, in Pierce and Maglieri (1972) and Piacsek (2002).

Second, we consider the propagation of a plane wavefront over a terrain depression with two different depths in Figs. 6(e) and 6(f). For the terrain depression of small depth in Fig. 6(e), the two mechanisms discussed above are at play: the wavefront is first bent outward above the downward slope of the terrain depression and then inward above the upward slope. This induces a cusp caustic as depicted in Fig. 6(d). The depth of the terrain depression in Fig. 6(f) is larger and corresponds to the geometry investigated in Emmanuelli *et al.* (2021). Note that a detailed analysis of the boom reflection was performed for this case in Emmanuelli *et al.* (2021); in particular, pressure maps from a numerical solution of the Euler equations and the wavefronts determined using a ray-tracing approach were compared. Due to the larger curvature of the terrain, the focal point appears closer to the ground than that in Fig. 6(e), and the lower branch of the caustic is reflected at the ground. As a result, a section of the ground along the upward slope of the terrain depression is in the illuminated zone of the caustics, and because of the reflection at the ground, there are five contributions to the reflected wavefront. In Emmanuelli *et al.* (2021), it was observed that the largest sonic boom noise levels along the ground are obtained in this zone.

IV. NUMERICAL RESULTS

A. T1—Mild slope

The results of the numerical simulations are first analyzed for ground profile T1, which presents mild slopes.

1. Overview

Maps of the pressure fluctuation p' are shown at different instants in time in Fig. 7 for the N-wave. The video showing the evolution of the N and C25D waves along ground profile T1 is available in Mm. 1. The maps are illustrative of topographic effects on boom reflection, which is detailed in Sec. III. First, note that the incident boom, injected at the right boundary of the domain, is the same for all the maps, contrary to the reflected boom.

Mm. 1. Video showing sonic boom propagation over ground profile T1 for (left) the N-wave and (right) the C25D wave.

For a locally constant slope, the reflected boom does not differ much from that above flat ground. The reflected boom wavefront is, thus, straight, as shown in Figs. 7(d) and

https://doi.org/10.1121/10.0019938

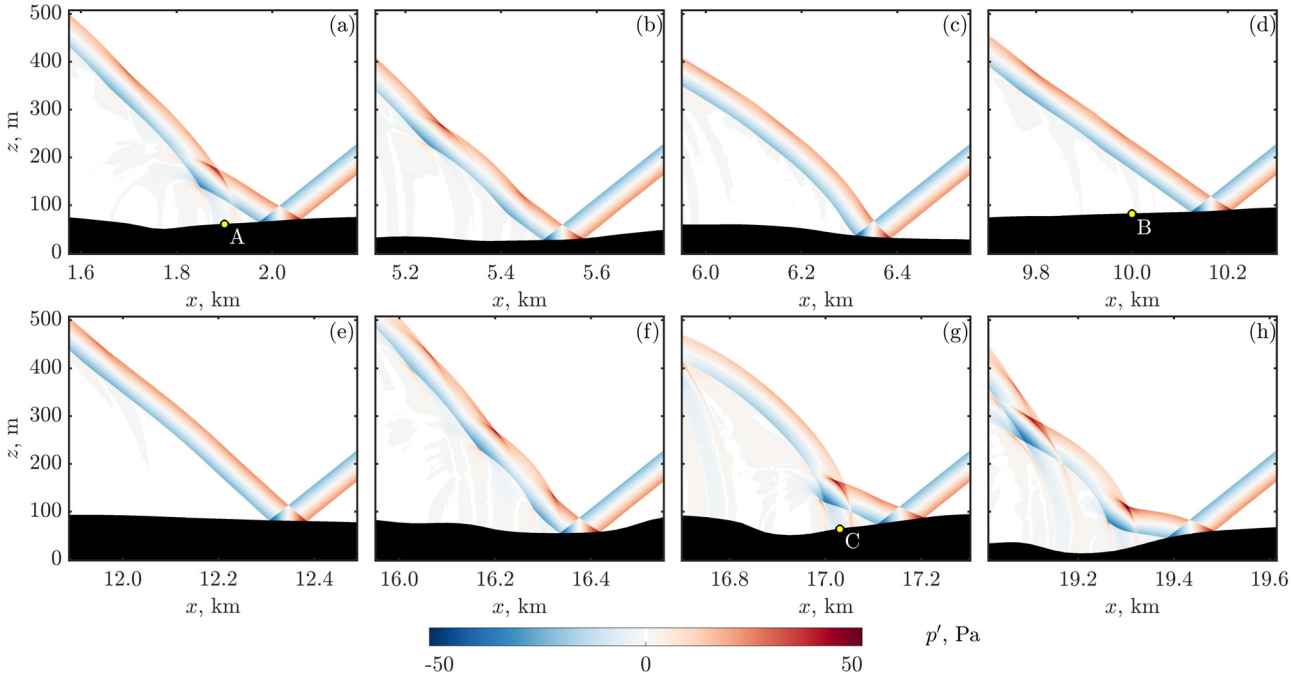

FIG. 7. (Color online) Pressure fluctuation maps at different instants in time for the *N*-wave and ground profile T1. The yellow dots indicate the positions at which the time signals in Fig. 8 are recorded.

7(e) for region T1b. Note that the angle of the reflected wavefront with respect to the horizontal depends on the slope angle because of specular reflection.

For locally curved terrain, the reflected boom wavefront is also curved. The curvature of the wavefront is directly related to that of the terrain. Thus, for locally convex terrain, the reflected boom wavefront is bent outward as illustrated in Fig. 7(c). On the contrary, for a locally concave terrain, the wavefront is bent inward, which induces folding of the reflected boom wavefront. A single folding with a distinctive butterfly shape can be observed above a terrain depression in Figs. 7(a) and 7(g). The folding is stronger in Fig. 7(g) for region T1c than it is in Fig. 7(a) for region T1a because of the larger curvature of the terrain. Moreover, in addition to the reflected boom, folding induces an additional contribution near the ground in Fig. 7(g) around $x = 17$ km, which is hardly visible in Fig. 7(a). In the case of successive terrain depressions, multiple folding of the wavefront occurs. Thus, the wavefront is folded twice in Figs. 7(b) and 7(h) and three times in Fig. 7(f).

2. Pressure waveforms

Time signals of the acoustic pressure are shown at three locations at ground level for the profile T1 in Fig. 8, for the *N*- and C25D waves. They are plotted as a function of $\tau = t - t_0$, where t is the time and t_0 is the time at which the acoustic pressure is first larger than 0.1 Pa. Points *A* and *C*, at $x = 1.9$ and 17 km, respectively, are located in zones where the greatest noise levels are obtained for regions T1a and T1c. They are situated along the uphill side on a terrain depression. First, the signals are composed of the incident

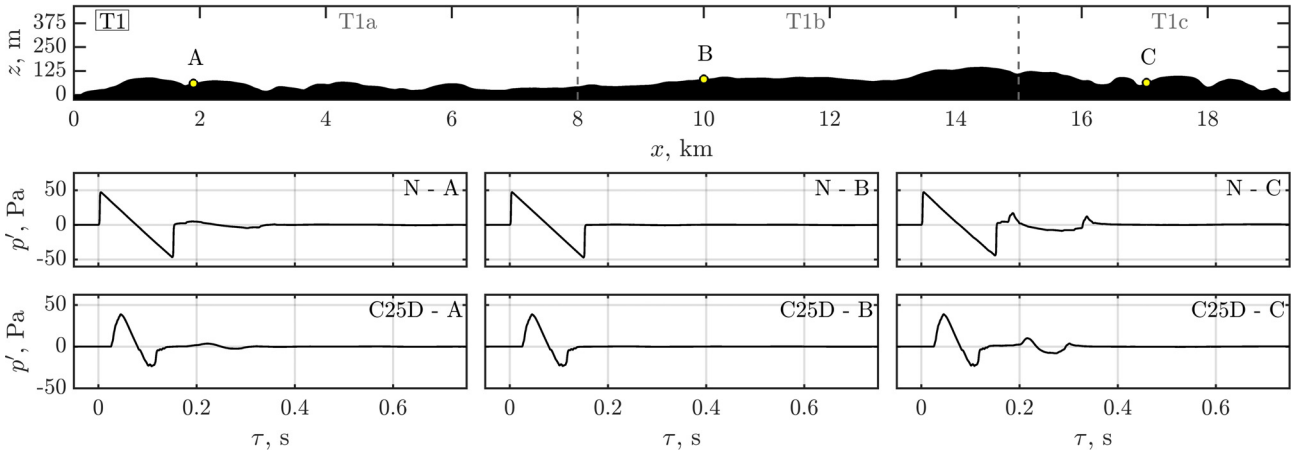

FIG. 8. (Color online) Time signals of the acoustic pressure at three positions along the ground profile T1 for (middle) the *N*-wave and (bottom) the C25D wave.

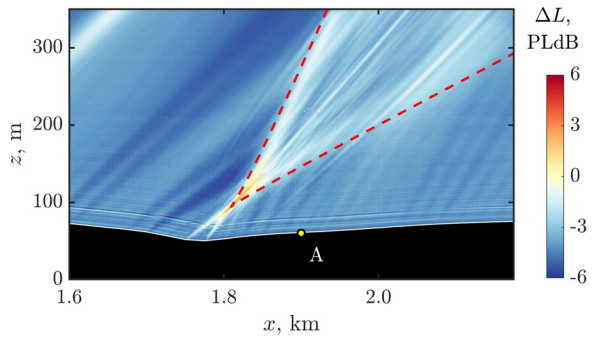

FIG. 9. (Color online) Map of the normalized noise levels, ΔL, using the metric PL for the C25D wave above the terrain depression at $x = 1.8$ km along profile T1. The caustics are overlaid with red dashed lines.

boom and its reflection at $\tau = 0$ and then of the contribution resulting from wavefront folding around $\tau = 0.2$ s, which can be observed in Figs. 7(a) and 7(g). The amplitude of the latter is larger at point C than at point A. This agrees with the observations made earlier about Figs. 7(a) and 7(g). However, the amplitude remains small compared to that of the incident boom. For the N-wave, this additional contribution appears as a U-wave. For point B in region T1b, the time signal is very close to that for the ideal case of a flat ground. After the contributions caused by the incident and reflected booms ($\tau > 0.2$ s), the acoustic pressure is, thus, almost zero. While the signal at point B is only an example, these remarks are valid for all the signals recorded at ground level in region T1b.

3. Noise levels

Figure 9 shows a map of the normalized noise levels, $\Delta L = L - L(\text{flat})$, for which the value at ground level in the case of a flat surface is used as a reference. It represents the terrain depression at $x = 1.8$ km along profile T1 with the C25D wave using the PL metric. Note that the acoustic field for the N-wave above this part of the profile is shown in Fig. 7(a). As a preliminary indication and compared to its value at the ground, the noise level above a flat surface decreases rapidly by 3 PLdB in the direction normal to the ground as mentioned in Dragna *et al.* (2022a) and also reported in Downs *et al.* (2022). Thus, the expected value of the normalized noise level is around -3 PLdB above a flat surface.

We observe in Fig. 9 that the normalized noise level is also around -3 PLdB overall above a non-flat ground. A notable increase in noise levels can be noted above the terrain depression at $x = 1.8$ km. To confirm that it is the result of focusing by the topography, a ray-tracing computation (Candel, 1977; Gainville, 2008; Scott *et al.*, 2017) has been performed, allowing us to determine the caustics, which are overlaid on the noise map in Fig. 9 with dashed lines. A cusp caustic is observed above the terrain depression, and the caustic branches closely match the regions with the greatest noise levels. In particular, the largest increase, by 3 PLdB, is obtained near the focal point. In addition, note that the noise level decreases above the ground at $x = 1.6$ or 1.7 km due to the local convexity of the ground.

The noise levels at ground level are now plotted along ground profile T1 in Fig. 10 for N and C25D waves. While noticeable noise level variations can be observed above the ground as shown in Fig. 9, the noise levels at ground level are globally not affected by the topography of profile T1. In detail, the difference in the noise levels is negligible for regions T1a and T1b. For T1c, the difference is visible but small: it only reaches 1 dB locally. Note that these conclusions are valid for both boom waves and CSEL and PL metrics for the C25D wave.

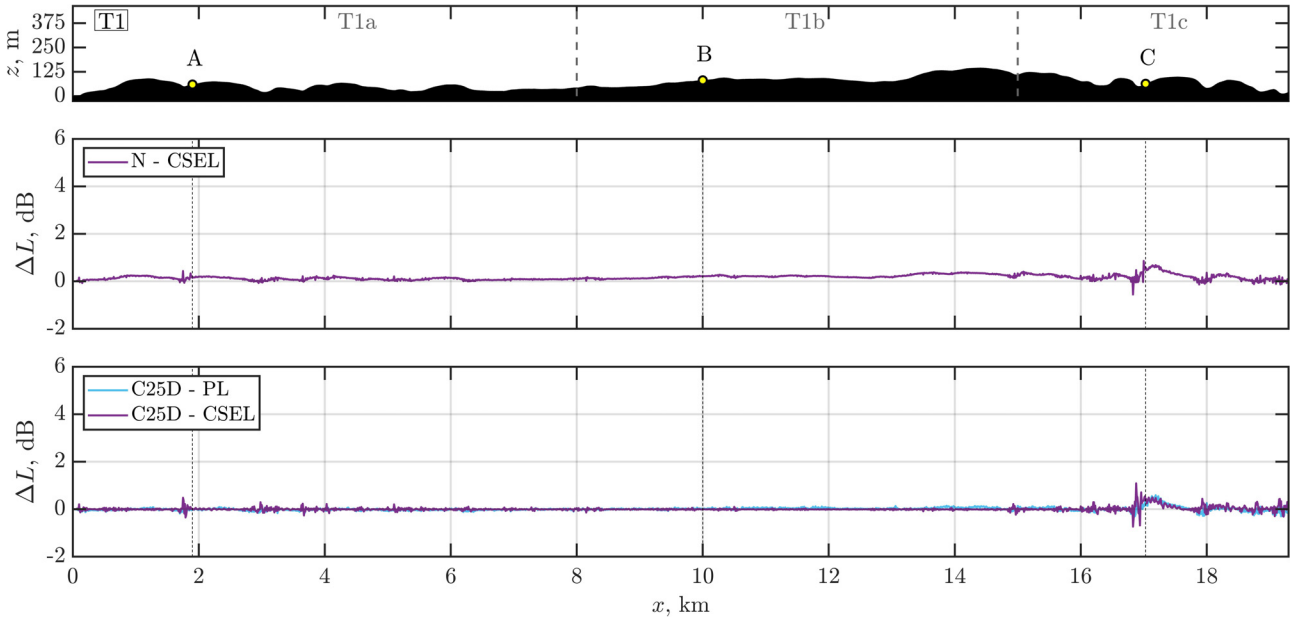

FIG. 10. (Color online) Perceived noise levels computed at ground level for profile T1 using PL and CSEL normalized by the flat surface case for (middle) the N-wave and (bottom) the C25D wave. The vertical dashed lines indicate the locations at which the time signals in Fig. 8 are recorded.

https://doi.org/10.1121/10.0019938

As a conclusion, although the acoustic field is significantly affected, a moderate topography does not modify noise levels at ground level compared to flat ground.

B. T2—Steep slope

Results are now considered for ground profile T2, that presents steeper slopes than T1.

1. Overview

Pressure fluctuation maps are shown at different instants in time for ground profile T2 and the *N*-wave in Fig. 11. The video showing the evolution of the *N* and C25D waves along profile T2 is available in Mm. 2. In Figs. 11(a)–11(e), 11(g), and 11(h), the maps are plotted above terrain depressions with steeper slopes than those of profile T1. As a consequence, the reflected wavefront is much more distorted as compared to Fig. 7. Furthermore, the magnitude of the folded wavefront reaching the ground is significant: see, for instance, Fig. 11(d) for which the amplitude of the folded wavefront near the ground at $x = 5.1$ km is comparable to that of the incident boom.

Mm. 2. Video showing sonic boom propagation over ground profile T2 for (left) the *N*-wave and (right) the C25D wave.

In addition, due to the rapid and significant variation of the elevation height for ground profile T2, multiple folding of the wavefront occurs for all the maps. In particular, a secondary folded wavefront can be noticed propagating near the ground in Fig. 11(c) at $x = 4.4$ km or Fig. 11(e) at $x = 5.5$ km.

Finally, Fig. 11(f) displays the pressure fluctuation map above the plateau located between 6.2 and 8 km. Double folding of the reflected boom wavefront is observed. However, the reflected wavefront is almost straight, and the acoustic energy near the ground remains small once the incident boom and its reflection have passed. Therefore, as noticed for ground profile T1, it is expected that the time signal at the ground and corresponding noise levels will not deviate significantly from those on a flat surface.

2. Pressure waveforms

Time signals at ground level are displayed in Fig. 12 at different locations along profile T2 with the *N*-wave. Waveforms at points *D*, *E*, *G*, *H*, *J*, *K*, and *L* are those for which the noise levels are the largest. As for ground profile T1, they are obtained on the upward slope of a terrain depression. The contribution resulting from wavefront folding appears as a *U*-wave. Depending on the geometry, the *U*-wave is included within the *N*-wave as at points *G* and *J*, follows the *N*-wave as at points *D*, *E*, *K*, or *L*, or arrives largely delayed compared to the *N*-wave, as at point *H*. Note also that secondary contributions due to multiple folding of the wavefront are noticed in the time signals at point *D* after $\tau > 0.4$ s and at point *G* after $\tau > 0.55$ s.

Compared to the waveforms obtained with profile T1 in Fig. 8, the amplitude of the contributions due to wavefront folding is much more significant. As an example, the peak pressure of the *U*-wave at point *L* is about 70 Pa, which is almost three times larger than that of the incident boom. This amplification is caused by the curvature of the terrain profile, which is greater for profile T2 than for T1: as a rule of thumb, it induces a stronger focusing. In the same line of

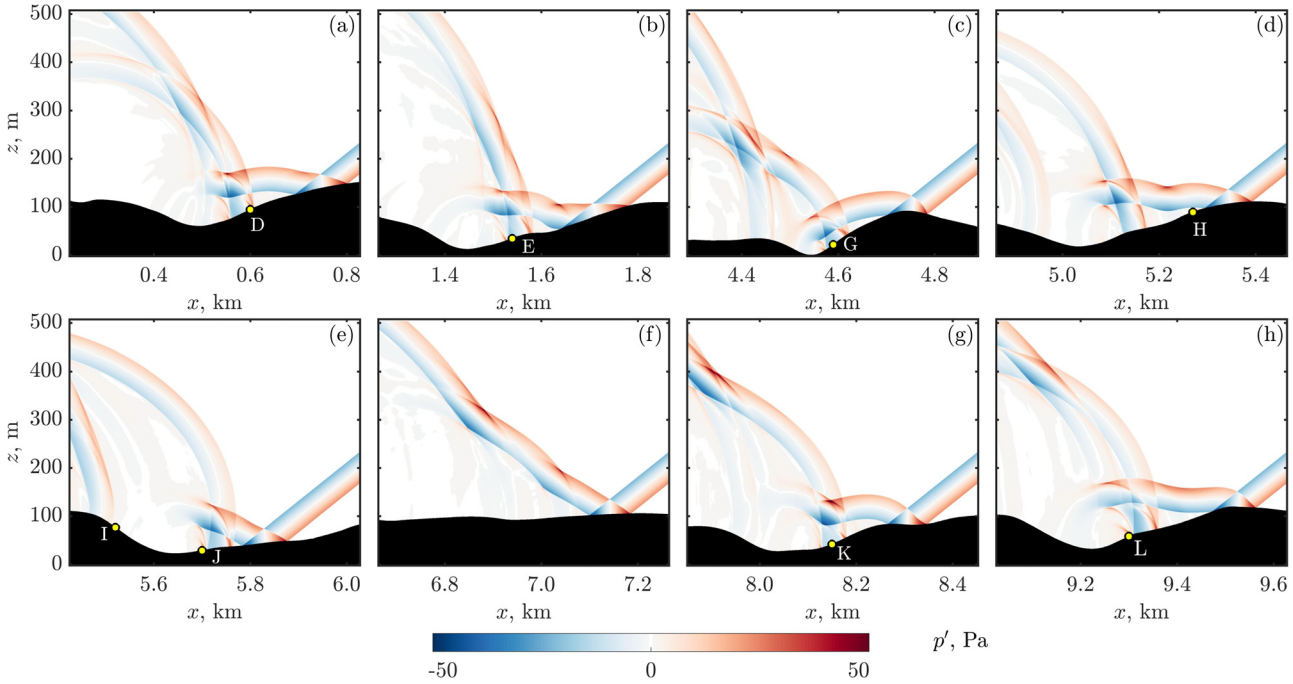

FIG. 11. (Color online) Pressure fluctuation maps at different instants in time for the *N*-wave and ground profile T2. The yellow dots indicate the positions at which the time signals in Fig. 12 are recorded.

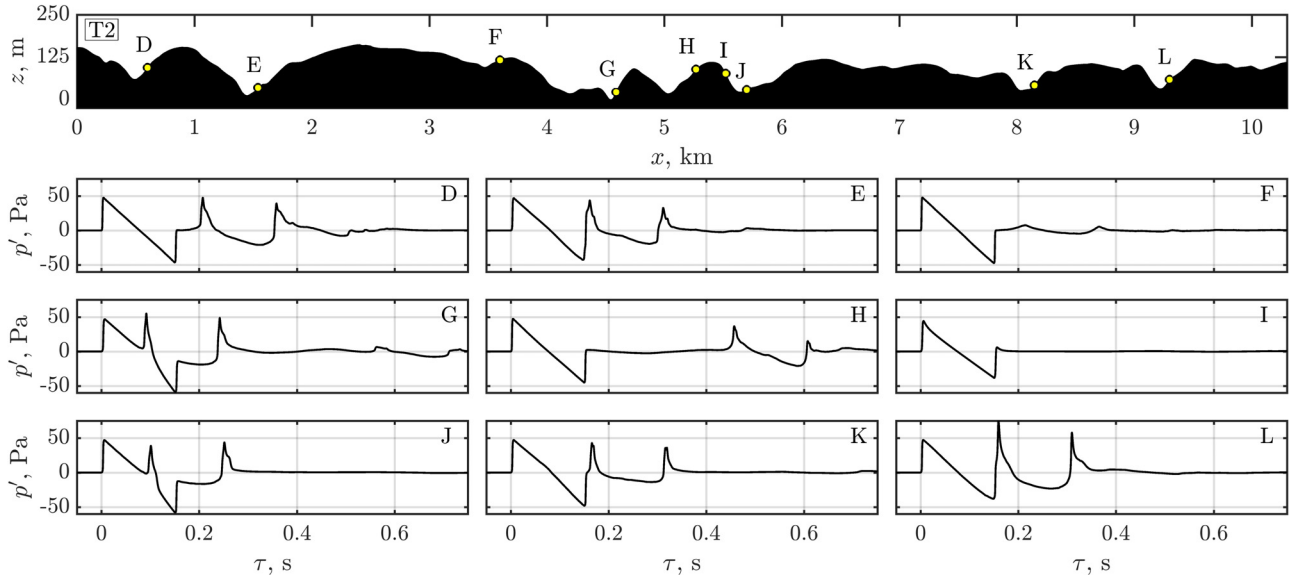

FIG. 12. (Color online) Time signals of the acoustic pressure at nine positions along ground profile T2 with the *N*-wave.

thought, the waveform at point *F* is obtained at a terrain depression but with a smaller curvature, similar to those of ground profile T1; in this case, the amplitude of the *U*-wave is comparable to that at points *A* and *C* in Fig. 8.

Finally, the time signal at point *I* is the one yielding the lowest noise levels along ground profile T2. Note that the point *I* is located downslope in between points *H* and *J* for which the noise levels are maximum. The waveform at point *I* looks like the incident *N*-wave. However, the time signal has a reduced energy compared to that on a flat surface with positive and negative peak pressures of 44.5 and −38 Pa instead of ±48 Pa.

3. Noise levels

An illustration of the noise level map obtained with ground profile T2 is depicted in Fig. 13(a) above the terrain depression at $x = 500$ m. As for Fig. 9, the normalized noise levels, ΔL, which use the noise level at ground level for the flat surface case as a reference, are plotted for the C25D wave using the PL metric. Note that the map of the instantaneous sound pressure for the *N*-wave is shown at the same location in Fig. 11(a). Compared to Fig. 9, the variation of the noise levels is more significant. To help the interpretation of the noise map, the caustics are computed with a ray-tracing code. For readability, they are not superimposed on to the noise map but are plotted in Fig. 13(b).

There are four regions where the noise levels are amplified by the topography. The first region is around $x = 300$ m and $z = 200$ m due to the curvature of the terrain at $x = 100$ m. The second region, near $x = 250$ m and $z = 120$ m, is generated by the moderate terrain depression located just below. The largest noise levels, with a maximum increase of 4.5 PLdB, are observed above the large terrain depression around $x = 500$ m. The caustic pattern induced by the topography is quite complex. There are two notable focal points, the first is close to the ground at $x = 485$ m and $z = 72$ m and the second is at a higher height at $x = 555$ m and $z = 143$ m. Note that the lower caustic branch associated with the focal point close to the ground is reflected on the ground at $x = 550$ m near point *D*. As discussed in Sec. III, this leads to the receivers below the reflected caustic branch being in the illuminated zone of the caustics with increased acoustic energy. Finally, a moderate increase in noise levels is observed above the ground at $x = 700$ m, which is the result of the slight terrain depression at the same position.

It can be noted that the caustics closely correspond to the regions of significant noise levels. In particular, the largest noise levels are obtained near the focal points.

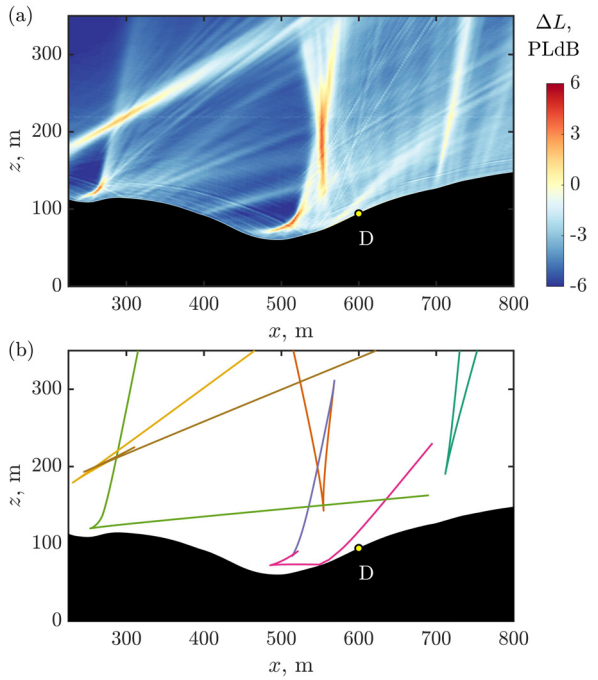

FIG. 13. (Color online) (a) Map of the normalized noise levels, ΔL, using the metric PL for the C25D wave above the terrain depression at $x = 500$ m along profile T2 and (b) corresponding caustics are depicted.

https://doi.org/10.1121/10.0019938

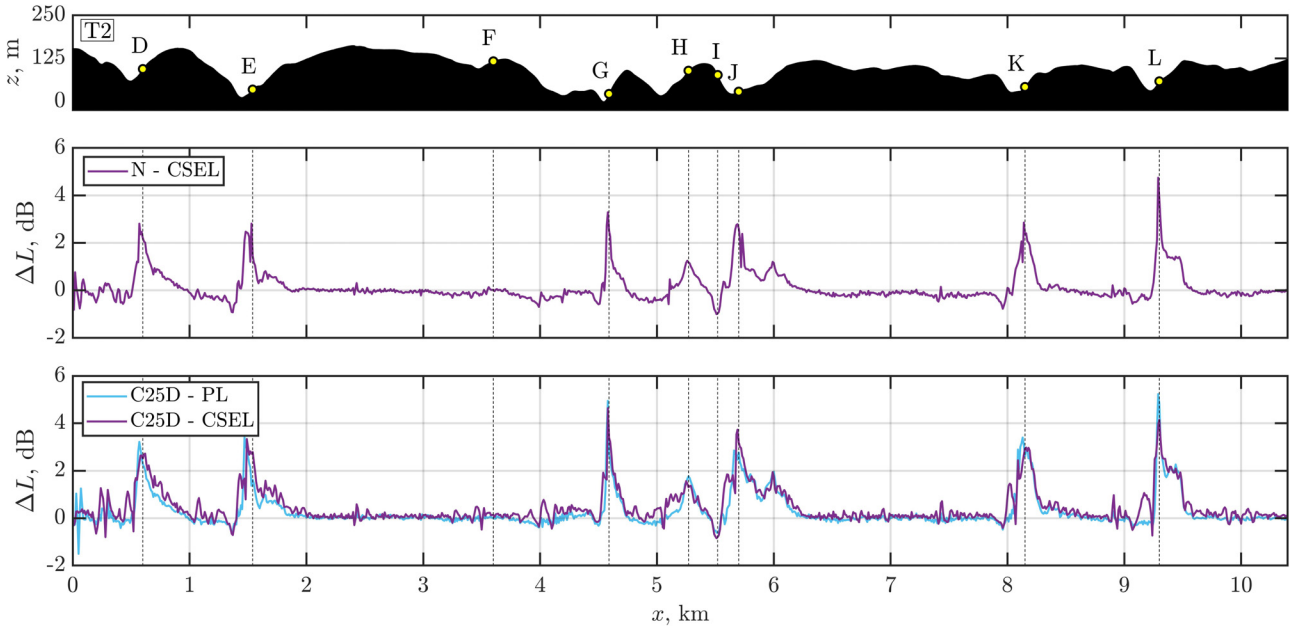

FIG. 14. (Color online) Perceived noise levels computed at ground level for profile T2 using PL and CSEL normalized by the flat surface case with (middle) the *N*-wave and (bottom) the C25D wave. The vertical dashed lines indicate the locations at which the time signals in Fig. 12 are recorded.

The noise levels at ground level normalized by the flat surface case are plotted along the ground profile T2 in Fig. 14. In agreement with the remarks made for profile T1 in Sec. IV A 3, the noise levels are close to zero in the regions that are nearly flat or have a moderate slope; this is observed, in particular, along the plateaus between $x = 2$ and 4 km and $x = 6.2$ and 8 km. The noise levels increase significantly close to the terrain depressions noted above. The maximum is obtained at $x = 9.3$ km with an increase by 5 dBC for the *N*-wave and 4 dBC and 5 PLdB for the C25D wave. There are also some locations for which the noise levels are slightly reduced compared to the flat case (see, e.g., $x = 1.4$ or 5.5 km). However, the reduction remains small: less than -0.5 dB for CSEL and PL metrics. Note that a large reduction in noise levels could be observed if the topography induced shadow zones; as discussed in Sec. III, this requires a slope smaller than -125% for a Mach number of 1.6 while the slope remains above -75% along ground profile T2. Overall, variations in topography tend to increase the noise levels. In addition, as already observed for the profile T1, the variation in noise levels is similar for both boom waves, and the CSEL and PL metrics give similar values for the C25D wave.

C. Statistical analysis

The cumulative probability distribution of the normalized noise levels at ground level is shown in Fig. 15 for the two profiles and two boom waves to estimate the occurrence in the variations in noise levels due to topography. For profile T1, as indicated in Sec. IV A 3, there is almost no change in the noise levels compared to the flat ground case, and the cumulative probability distribution corresponds to a vertical line around zero. For profile T2, the cumulative probability distribution is more spread out, especially toward positive values of normalized noise levels. Moreover, it is similar for the different metrics and incident boom waves used. An increase by more than 2 dB occurs for 5% of the receivers at ground level, and for approximately 1% of them, the noise levels are amplified by more than 3 dB.

V. CONCLUSIONS

Sonic boom propagation over real topography has been investigated. Numerical simulations based on the 2D Euler equations were performed for two ground profiles, extracted from topographical data of hilly regions, and for two boom waves, an *N*-wave and a low-boom wave. For the first ground profile with mild slopes (30% at maximum), the acoustic field is significantly affected by topography. In particular, wavefront folding was observed each time the

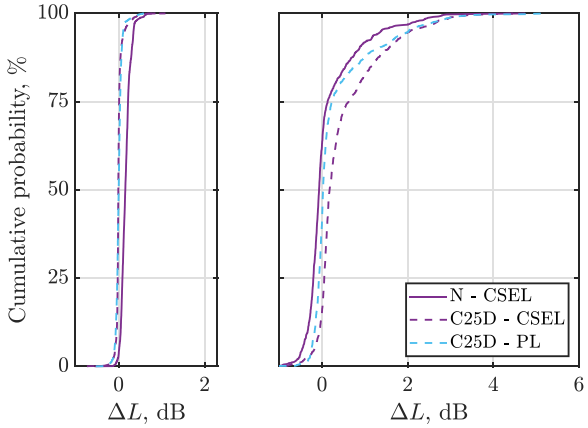

FIG. 15. (Color online) Cumulative probability distributions of the perceived noise levels at ground level normalized by the flat surface case for ground profiles (left) T1 and (right) T2 are shown.

incident boom reflects on a terrain depression. The time signals of the acoustic pressure at ground level were, however, rather unaffected, and the corresponding noise levels deviate from the flat terrain reference by less than 1 dB. An important conclusion is that moderate topography does not play a significant role on the noise levels at ground level. For the second ground profile with steep slopes (80% at maximum), the effect of topography is amplified. In particular, the time signals of the acoustic pressure at the ground in the vicinity of terrain depressions present extra contributions of noticeable amplitude in addition to the incident and reflected booms, resulting in an increase in the noise levels. For the profile considered, the noise levels were amplified by more than 3 dB for 1% of the ground surface area, and a maximum increase of 5–6 dB was reached.

There are several possible extensions to this work. The main assumption of this study is the restriction to 2D geometries. Therefore, it would be worthwhile to account for three-dimensional effects. Although the results are expected to be qualitatively similar, the noise levels might differ by a few decibels. In addition, we consider perfectly reflecting ground: a direct continuation of this work would be to extend the analysis to absorbing ground. Also, the effect of ground roughness on sonic boom reflection could be investigated. Note that this would require having elevation data with finer resolution than currently available or generating the roughness profile from statistical models. Finally, the atmosphere was homogeneous and at rest. Topography plays an important role on the atmospheric boundary layer. It would be interesting to investigate the joint effect of topography and meteorological conditions on boom reflection as temperature and wind speed gradients will modify the boom incidence angle as well as the location of caustics.

ACKNOWLEDGMENTS

This project has received funding from the European Union's Horizon 2020 research and innovation programme under Grant agreement No. 769896 (RUMBLE). This publication reflects only the author's view and the Innovation and Networks Executive Agency (INEA) is not responsible for any use that may be made of the information it contains. It was performed within the framework of the LABEX CeLyA (ANR-10-LABX-0060) of Université de Lyon within the program "Investissements d'Avenir" (ANR-16-IDEX-0005) operated by the French National Research Agency (ANR). This work was granted access to the high performance computing resources of PMCS2I (Pôle de Modélisation et de Calcul en Sciences de l'Ingénieur et de l'Information) of Ecole Centrale de Lyon, member of FLMSN (Fédération Lyonnaise de Modélisation et Sciences Numériques), partner of EQUIPEX EQUIP@MESO, and IDRIS (Institut du Développement et des Ressources en Informatique Scientifique) under the allocation 2020–02203 made by GENCI (Grand Equipement National de Calcul Intensif). The authors declare no conflicts of interest. Data from numerical simulations are available from the authors on reasonable request.

Bauer, A. B., and Bagley, C. J. (**1970**). "Sonic boom modeling—Investigation of topographical and atmospheric effects," McDonnel-Douglas Corp., Long Beach, CA, Rep. No. FAA-NO-70-10, pp. 1–212.

Blumrich, R., Coulouvrat, F., and Heimann, D. (**2005**). "Meteorologically induced variability of sonic-boom characteristics of supersonic aircraft in cruising flight," J. Acoust. Soc. Am. **118**(2), 707–722.

Bogey, C., and Bailly, C. (**2004**). "A family of low dispersive and low dissipative explicit schemes for flow and noise computations," J. Comput. Phys. **194**, 194–214.

Candel, S. (**1977**). "Numerical solution of conservation equations arising in linear wave theory: Application to aeroacoustics," J. Fluid Mech. **83**(3), 465–493.

Carr, A. N., Lonzaga, J. B., and Miller, S. A. E. (**2022**). "Numerical prediction of loudness metrics for *N*-waves and shaped sonic booms in kinematic turbulence," J. Acoust. Soc. Am. **151**(6), 3580–3593.

Downs, R., Page, J. T., Gee, K. L., Novakovich, D. J., Anderson, M. C., and Loubeau, A. (**2022**). "Sonic boom measurements: Practical implications considering ground effects, microphone installation, and weather hardening," JASA Express Lett. **2**(10), 104001.

Dragna, D., Emmanuelli, A., Ollivier, S., and Blanc-Benon, P. (**2022a**). "Sonic boom reflection over an isolated building and multiple buildings," J. Acoust. Soc. Am. **151**(6), 3792–3806.

Dragna, D., Emmanuelli, A., Ollivier, S., and Blanc-Benon, P. (**2022b**). "Sonic boom reflection over urban areas," J. Acoust. Soc. Am. **152**(6), 3323–3339.

Emmanuelli, A., Dragna, D., Ollivier, S., and Blanc-Benon, P. (**2021**). "Characterization of topographic effects on sonic boom reflection by resolution of the Euler equations," J. Acoust. Soc. Am. **149**(4), 2437–2450.

Gainville, O. (**2008**). "Modélisation de la propagation atmosphérique des ondes infrasonores par une méthode de tracé de rayons non linéaire" ("Numerical modelling of atmospheric infrasound propagation using a nonlinear ray-tracing method"), Ph.D. thesis, Ecole Centrale de Lyon, France, No. 2008-07.

Gal-Chen, T., and Sommerville, R. C. J. (**1975**). "On the use of a coordinate transformation for the solution of the Navier-Stokes equations," J. Comput. Phys. **17**, 209–228.

Leal, P. B. C., Schrass, J. A., Giblette, T. N., Hunsaker, D. F., Shen, H., Logan, T. S., and Hartl, D. J. (**2021**). "Effects of atmospheric profiles on sonic boom perceived level from supersonic vehicles," AIAA J. **59**(12), 5020–5028.

Leatherwood, J. D., Sullivan, B. M., Sheperd, K. P., McCurdy, D. A., and Brown, S. A. (**2002**). "Summary of recent NASA studies of human response to sonic booms," J. Acoust. Soc. Am. **111**(1), 586–598.

Leconte, R., Chassaing, J. C., Coulouvrat, F., and Marchiano, R. (**2022**). "Propagation of classical and low booms through kinematic turbulence with uncertain parameters," J. Acoust. Soc. Am. **151**(6), 4207–4227.

Loubeau, A., and Coulouvrat, F. (**2009**). "Effects of meteorological variability on sonic boom propagation from hypersonic aircraft," AIAA J. **47**(11), 2632–2641.

Loubeau, A., Naka, Y., Cook, B., Sparrow, V., and Morgenstern, J. (**2015**). "A new evaluation of noise metrics for sonic booms using existing data," AIP Conf. Proc. **1685**, 0090015.

Maglieri, D., Bobbitt, P., Plotkin, K., Shepherd, K., Coen, P., and Richwine, D. (**2014**). "Sonic boom: Six decades of research," Technical Report NASA/SP-2014-622, L-20381, NF1676L-18333 (NASA, Washington, DC), pp. 1–539.

NASA (**2022**). "Quesst," X-59, NASA's low-boom flight demonstration, available at https://www.nasa.gov/X59/ (Last viewed June 1, 2023).

Pawlowski, J., Graham, D., Boccadoro, C., Coen, P., and Maglieri, D. (**2005**). "Origins and overview of the shaped sonic boom demonstration program," in *43rd AIAA Aerospace Sciences Meeting and Exhibit*, 10–13 January, Reno, NV, AIAA-Paper No. 2005-5, pp. 1–14.

Piacsek, A. A. (**2002**). "Atmospheric turbulence conditions leading to focused and folded sonic boom wave fronts," J. Acoust. Soc. Am. **111**(1), 520–529.

Pierce, A. D., and Maglieri, D. J. (**1972**). "Effects of atmospheric irregularities on sonic-boom propagation," J. Acoust. Soc. Am. **51**(2), 702–721.
Rallabhandi, S. K., and Loubeau, A. (**2019**). "Summary of propagation cases of the second AIAA sonic boom prediction workshop," J. Aircraft **56**(3), 876–895.
Scott, J. F., Blanc-Benon, P., and Gainville, O. (**2017**). "Weakly nonlinear propagation of small-wavelength, impulsive acoustic waves in a general atmosphere," Wave Motion **72**, 41–61.
Stevens, S. S. (**1972**). "Perceived level of noise by Mark VII and decibels (E)," J. Acoust. Soc. Am. **51**(2), 575–601.
Stout, T. A., Sparrow, V. W., and Blanc-Benon, P. (**2021**). "Evaluation of numerical predictions of sonic boom level variability due to atmospheric turbulence," J. Acoust. Soc. Am. **149**(5), 3250–3260.
Yamashita, H., and Obayashi, S. (**2013**). "Global sonic boom overpressure variation from seasonal temperature, pressure, and density gradients," J. Aircraft **50**(6), 1933–1938.